A Minimally Invasive Multimodality Image-Guided (MIMIG) Molecular Imaging System for Peripheral Lung Cancer Intervention and Diagnosis

Tiancheng He[1,2], Zhong Xue[1], Kelvin K. Wong[1], Miguel Valdivia y Alvarado[1], Yong Zhang[1], Weixin Xie[2], and Stephen T.C. Wong[1]

[1] The Center for Bioengineering and Informatics, The Methodist Hospital Research Institute and Department of Radiology, The Methodist Hospital, Weil Cornell Medical College, Houston, Texas, USA
[2] Intelligent Information Institute, Shenzhen University, Shenzhen, China
zxue@tmhs.org

Abstract. The once-promising computed tomography (CT) lung cancer screening appears to result in high false positive rates. To tackle the common difficulties in diagnosing small lung cancer at an early stage, we developed a minimally invasive multimodality image-guided (MIMIG) interventional system for early detection and treatment of peripheral lung cancer. The system consists of new CT image segmentation for surgical planning, intervention guidance for targeting, and molecular imaging for diagnosis. Using advanced image segmentation technique the pulmonary vessels, airways, as well as nodules can be better visualized for surgical planning. These segmented results are then transformed onto the intra-procedural CT for interventional guidance using electromagnetic (EM) tracking. Diagnosis can be achieved at microscopic resolution using a fiber-optic microendoscopy. The system can also be used for fine needle aspiration biopsy to improve the accuracy and efficiency. Confirmed cancer could then be treated on-the-spot using radio-frequency ablation (RFA). The experiments on rabbits with VX2 lung cancer model show both accuracy and efficiency in localization and detecting lung cancer, as well as promising molecular imaging tumor detection.

Keywords: image-guided intervention, peripheral lung cancer, image computing, molecular imaging.

1 Introduction

Lung cancer is the most common cause of cancer-related death in men and women. The American Cancer Society estimated over 210,000 new lung cancers and about 160,000 deaths from lung cancer for the United States in 2007. Deaths from lung cancer in the nation outnumbered the cumulative deaths from colon, breast, and prostate cancers. Peripheral lung cancer constitutes more than half of all lung cancer cases. However, computed tomography (CT) diagnosis is known to result in high false positive rates to confirm malignancy [1] (most studies reported false positive

N. Navab and P. Jannin (Eds.): IPCAI 2010, LNCS 6135, pp. 102–112, 2010.

rates between 10% and 20% [2]). It is believed that the key to improving long term survival rate of patients with lung cancer is early detection, accurate localization and diagnosis, and novel therapies [1, 3]. The Mayo Clinic experience shows that when high risk individuals are screened for lung cancer with CT, the likelihood that they undergo a thoracic resection for lung cancer is increased by 10-fold [4]. To tackle the common difficulties in identifying small lung lesions (<1.5cm) at an early stage, an image-guided therapy approach is most promising.

In this paper, we introduce a minimally invasive multimodality image-guided (MIMIG) intervention system for early detection of peripheral lung cancer. The approach relies on initial pre-procedural CT imaging to locate small lesions. From the pre-procedural scan, pulmonary vessels, airways, as well as nodules can be segmented for better visualization during surgical planning, which can be transformed to intra-procedural scan using deformable registration for guiding the intervention. Electromagnetic (EM) tracking is embedded in the system to visualize the probe location in 3D CT, so physicians can efficiently perform the intervention by referring to the feedback from the visualization. After successfully targeting the lesion, fiber-optic molecular imaging is used for diagnosis through microendoscopy, and the confirmed malignant tumor can be treated immediately using radio-frequency ablation (RFA). MIMIG can also be used for fine needle aspiration biopsy to improve the accuracy and efficiency.

The proposed MIMIG system consists of the following components: 1) an electromagnetic (EM) tracking device for real-time tracking of the needle introducer; 2) coherent software for real-time localization and visualization of multiple devices being tracked on the intra-procedural CT images; 3) a fiber-optic microendoscope for fluorescence molecular imaging diagnosis and a radio-frequency ablation needle for localized therapy. New image computing modules are incorporated in the system for improved visualization and accuracy, and modular design of the functions in the Philips PMS Informatics Infrastructure (PII). PII is a commercial software development environment for the development, integration, deployment, monitoring and support of inter- and intra-enterprise healthcare solutions that deliver clinical functionality to the point of need, allowing us to implement these new functions conveniently through dynamic-link libraries. We hypothesize that MIMIG will allow us to accurately and efficiently detect small peripheral lung cancer and treat it at an earlier stage on-the-spot. In the experiments, the MIMIG system and the molecular imaging module have been validated using eight rabbit models, and the results show accuracy and efficiency in localization and detecting lung cancer.

2 The MIMIG System

2.1 System Overview

The MIMIG lung intervention system consists of one workstation for computing and visualization, an electromagnetic (EM) tracking system for localizing the position of the needle, a microendoscopy imaging system, and a needle-based treatment device such as radiofrequency ablation probe. The intervention and diagnosis is performed in the CT room. In this paper, we introduce and validate the MIMIG system using the

lung intervention experiments for live rabbits. Although MIMIG has been embedded with a molecular imaging system, it can also be applied to other applications such as image-guided biopsy and ablation for improving the accuracy and efficiency.

A. System hardware

In addition to the MIMIG workstation developed based on the PII platform, we adopt the NDI Aurora EM tracking system and the Valleylab Cool-tip ablation system for tracking the interventional probe and performing lung cancer treatment if necessary. CellVizio 660 fiber-optic microendoscopy system is utilized to capture the molecular images, and for this purpose the IntegriSense 680 fluorescent contrast agent is used to label $\alpha_v\beta_3$ integrin expressed in malignant cancer cells. During the past two years, we setup all the hardware and developed the software modules to complete a functional prototype system, and tested it on live rabbits. In another parallel study [5], we confirmed that the subcutaneous A547 nude mice tumor highly expresses $\alpha_v\beta_3$ integrin and labeled well with IntegriSense 680. This further supports the feasibility of applying MIMIG for lung cancer diagnosis.

Fig. 1 shows some pictures of the MIMIG system. The portable MIMIG system (Fig. 1(a)) can be used in the CT room to help physicians accurately guide the probe to the target and to perform precise molecular imaging, fine-needle biopsy, as well as radiofrequency ablation. In our experiments, the MIMIG system and the molecular imaging module have been validated using rabbit models, and Fig. 1 (b) shows a rabbit experiment. The rabbit experiments not only validate the accuracy and efficiency for localization of lung cancer using MIMIG system but also show the feasibility for detecting lung cancer using molecular imaging.

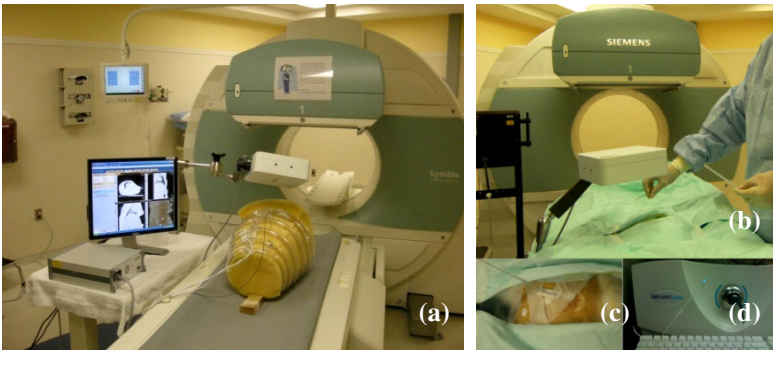

Fig. 1. System setting and interventional experiments. (a) The setting of the system; (b) rabbit intervention experiment; (c) picture of the probe; (d) the CellVizio system.

B. System workflow

The workflow paradigm of the image-guided diagnosis and therapy system is implemented by using a modular multimodality image guidance platform. In this system, peripheral lung cancer diagnosis is accomplished based on morphologic and molecular imaging information obtained from different imaging modalities. Fig. 2 illustrates the workflow of the MIMIG system. If the nodule size detected from CT is small, the MIMIG system will be used for further diagnosis or treatment. Traditional

method will be used for larger nodules. The MIMIG system is used to confirm the initial diagnosis using real-time fiber-optic fluorescence molecular imaging and to guide the treatment for the small lesions. After injection of optical contrast agent (e.g., IntegriSense 680) the MIMIG system can guide accurately the interventional needle to the right location, and molecular imaging diagnosis can be accomplished by using CellVizio 660 system. Our rationale is that high sensitivity and specificity diagnosis can be achieved for small peripheral lung cancer through accurate intervention and molecular imaging. Compared to the previous systems which focus on precise targeting using EM tracking [6-10], MIMIG not only provides new image computing modules but also presents an on-the-spot treatment solution so that the confirmed malignant lesion can be treated onsite by using radiofrequency ablation. MIMIG significantly shortens the duration between diagnosis and treatment and reduces the healthcare cost involved in this procedure.

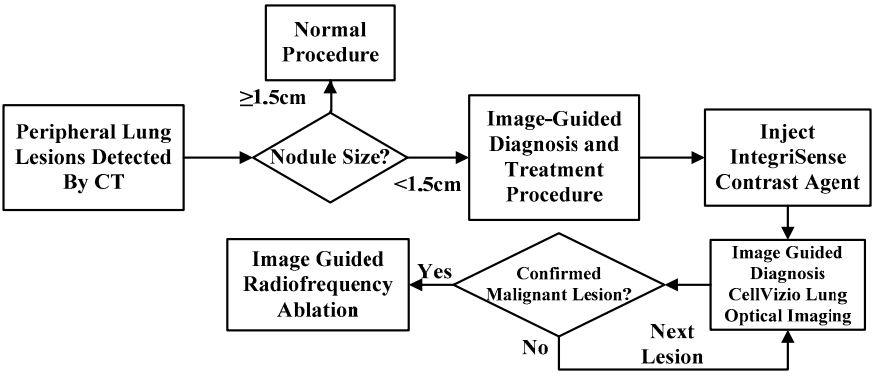

Fig. 2. The workflow of image-guided diagnosis and treatment for peripheral lung cancer

C. System software

The MIMIG software modules are constructed from the visual application builder of PII. PII enables one unified application development environment and provides implicit compatibility of shared components, which enables optimally tuned pre-clinical or clinical workflow. By using standardized interfaces, information models and API's, it provides the complete spectrum of applications between console and enterprise software, common schemas for configuration, preferences, and databases.

Standard informatics infrastructure and applications have been implemented in the PII system. The informatics infrastructure utilized in MIMIG includes workflow design, DICOM protocol, data input/output, and data repository. The standard applications that MIMIG used include 2D/3D visualization and interaction with the current workflow and imaging data, human interface functions, multi-modality image fusion, EM tracking and molecular imaging data stream interface.

Most importantly, PII allows extension of new components, thus our new image processing modules of the MIMIG system were implemented using based on this extendable feature. Fig. 3 illustrates how a new function is incorporated in the PII platform. For example, a new component in the new image segmentation can be first

constructed in the PII visual application builder using XML and C# languages. C# codes define the classes of the services that the segmentation component will provide, including data input, output, and functions. XML provides the properties of this component used by the PII visual application builder. Then the detailed implementation of the image segmentation function can be written either in C or C++ language and compiled as an external dynamic-link library (DLL). Finally the segmentation function can be easily called by using a program wrapper. In this way, any new functions can be easily embedded in the PII system, and used in the visual application builder to provide the flexibility of reconfiguring the MIMIG system.

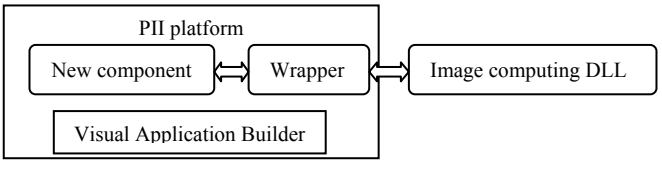

Fig. 3. Illustration of adding a new component/function to PII platform

Using PII platform we implement the real-time visualization and guidance functions for EM-based intervention tools. The major functions implemented include: 1) automatic lung field and vessel segmentation, as well as the visualization for path planning from pre-procedural images; 2) saving and loading the segmentation results and path planning data for intra-procedural use; 3) registering the pre-procedural image, segmentation results and the path planning data onto the intra-procedural images for better visualization; 4) visualization of the segmentation results of vessels and nodules in both volumetric and surface meshes; 5) image guidance based on the EM-tracking and CT images to determine the location of the needle in the CT image in different views; 6) enabling multiple devices (needles) tracking from the EM system and visualize them in the PII MIMIG system; and 7) performing data fusion between microendoscopy and the CT image-based guidance system.

2.2 Novel Software Modules and Features

We developed novel image computing tools including segmentation [11], registration [12], and microendoscopy image sequence processing for MIMIG. The pre-procedural images can be segmented for better visualization during surgical planning, and since fast segmentation is needed for intra-procedural images, the segmentation results will be transformed onto the intra-procedural images for visualization during the intervention. Using these tools fast and accurate image segmentation and registration algorithms are developed for better visualization during surgical planning and intervention, and alignment of pre-procedural and intra-procedural images; microendoscopy is used for lung cancer diagnosis, and cancerous lesions is treated on-the-spot using RFA. The software modules were implemented using C++ language as an external DLL and incorporated in to the PII platform. With properly designed software interface, they can also be embedded in other open-source platforms such as the Image-Guided Surgical Toolkit (IGSTK).

A. Lung field and blood vessel segmentation

A lung field and pulmonary vessel segmentation tool is developed for MIMIG. First, the background and the cavity areas are automatically detected using 3D region growing; then, 3D morphological operations are performed to filter out the noise and fill the holes in the segmentation results; finally, a novel Vascularity-Oriented LEvel Set (VOLES) algorithm [11] is proposed for pulmonary vessel segmentation. The results show it outperforms traditional level set method on pulmonary vessel segmentation. Using manual points in twenty patients the results show that that VOLES obtained sensitivity rate of 96% and specificity rate of 97% for our datasets.

B. Deformable registration of lung parenchyma

The alignment of the pre-procedural lung CT images as well as the intra-procedural images is an important step to accurately guide and monitor the interventional procedure. We devised a robust joint serial image registration and segmentation method [12], wherein serial images are segmented based on the current temporal deformations so that the temporally corresponding tissues tend to be segmented into the same tissue type. Note that the simultaneous registration and segmentation framework had been studied in [13-15] for MR images. The advantage of our new algorithm is that no temporal smoothness about the deformation field is enforced so that our algorithm can tolerate larger or discontinuous temporal changes that often appear during image-guided therapy. Moreover, physical procedure models could also be incorporated to our algorithm to better handle the temporal changes of the serial images during intervention. The proposed algorithm has been applied to both simulated and real serial lung CT images and compared it with the free-form deformation (FFD) [16]. The dataset used in the experiments consists of anonymized serial lung CT images of lung cancer patients. The results show that the proposed algorithm yields more robust registration results and more stable longitudinal measures: the mean registration error is $0.9mm$ for image resolution $0.7\times0.7\times1.5mm^3$, and is $4.1mm$ for images with resolution $0.81\times0.81\times5\ mm^3$.

C. Quantification of microendoscopy images

To reliably detect tumor tissue with molecular labeling, we perform temporal motion correction and scene change detection across the image sequences: a smooth temporal motion model is used to estimate the shifting and small rotation of the image sequence, and a scene change signal is generated if the degree of matching between two consequent frames is low. For motion correction a novel fluorescence microendoscopy motion correction (FMMC) algorithm using both of normalized mutual information (NMI) and augmented unscented Kalman filter (AUKF) is developed. Using this method, the similarity between consequent frames after serial image registration is defined by NMI, and the longitudinal transformation across the serial images is also subject to the regularization of AUKF. In this way, we can obtain relatively longitudinally stable transformations to correct the motion along the video. To optimize the combined objective function of NMI and AUKF, an iterative optimization algorithm is designed, and the parameters are adjusted to the microendoscopy image sequence alignment.

3 Experiments and Results

3.1 Materials

The protocol has been revised and approved by the Comparative Medicine Program at our institute, and all the procedures were carried in our facilities. The lung tumor models were created using females White New Zealand Rabbits, the animals had weights of 2.2kg±200g. The initial VX2 tumor cell line was provided by the department of comparative medicine at MD Anderson. In order to propagate this cell line in our facility a tumor cell suspension was first inoculated in the limb of one rabbit, a tumor with a diameter around 20*mm* was noticeable after two weeks. From this tumor two cell suspensions were prepared, one for limb inoculation and the other one for lung inoculation. For this procedure the rabbits were anesthetized with general anesthesia, and the hair of the thoracic was shaved completely. The lung inoculation was performed under fluoroscopy guidance. Once a region of the lung was selected an 18G Chiba needle was introduced in the rabbit chest. In order to simulate a peripheral lung tumor the needle was placed at the base of the right lung and the depth of the needle was continuously assessed with different fluoroscopy views of the C-arm at 0, 45 and 90 degrees. Once the needle was in the desire location and adequate depth the VX2 cell suspension was injected. Five minutes later new fluoroscopic images of the rabbit chest were taken for pneumothorax assessment. No animal developed pneumothorax in our experiments. The VX2 tumor size was assessed with weekly CT until a desired size of ~15*mm* was attained.

On the day of the image-guided diagnosis experiment the rabbit was anesthetized with general anesthesia and taken to the CT facility. A pre-procedural CT scan with breath holding was performed. The data was then transferred to the MIMIG system using the build in DCMTK tool. This CT scan was used for image segmentation, tumor identification and surgical planning. After placing five or six active fiducials near the chest of rabbit, the coordinates of the fiducials in the EM-tacking space and the CT image space were registered using affine transformation. During intervention real-time tracking data including the location and orientation of the intervention devices were precisely measured by the EM sensors and mapped onto the CT image space in real-time. For the guidance, the user-friendly visualization interface was used.

Fig. 4 (a) shows the interface for surgical planning where the target point is manually selected as the center of the tumor, and the entry point indicates the location for puncturing the needle. For the surgical planning the pre-procedural CT volume has been segmented using our advanced lung volume segmentation algorithm and the lung lesions were labeled and visualized in both volumetric and surface meshes. A surgical planning interface has been provided for the operator to interactively create a path for the needle insertion. The orthogonal viewer (simultaneous axial, sagittal, and coronal view) provided a clear perspective about the depth, and direction of the needle should be used for reaching the tumor. Before puncturing the needle, we confirmed the needle tracking accuracy and location at the point of entry and ensured the line traced between the point of entry (skin) and the target (tumor) was planned according to the orthogonal viewer. This must be consistent in all the views displayed on the screen. A small (3mm) incision was made at the skin level for the needle.

Before the puncture the animal was breath hold again, avoiding any movement from the chest. Fig. 4 (b) shows the interface indicating that the needle tip had reached the target. Once the tumor (target) was reached we proceed to needle fixation, preventing movement due to the CT gantry of respiratory movements that may displace the needle from the target location. A post-procedural scan with breath holding was performed to verify the needle location.

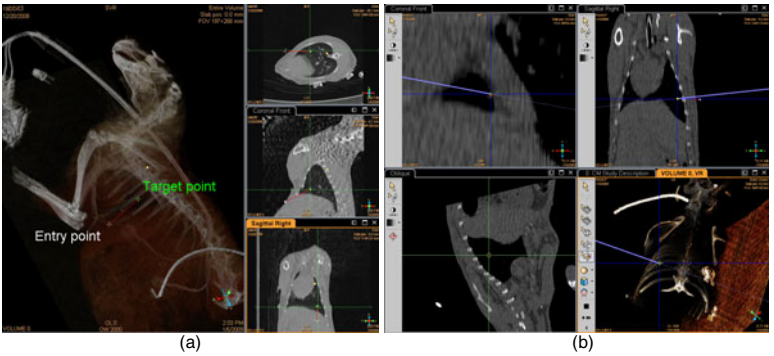

Fig. 4. Visualization design. (a) Visualization of surgical planning; (b) screen shot of image guidance during the rabbit experiments.

3.2 Performance Evaluation

To evaluate the accuracy of the needle intervention, we calculated the distance between the manually selected needled tip from the confirmation CT and the target point obtained during surgical planning. Since the rabbit might move from the pre procedural to post-procedural scan, a global image registration was performed afterwards. Fig. 5 (a) shows a screen cut of the tumor and the arrow points to the target point in the pre-procedural CT. Fig. 5 (b) gives the corresponding slice, and the arrow points to the needle tip in the confirmation CT. Fig. 5 (c) shows the registered image. After these steps, the distance between these two points can be calculated. The result can be translated as the needle puncture accuracy.

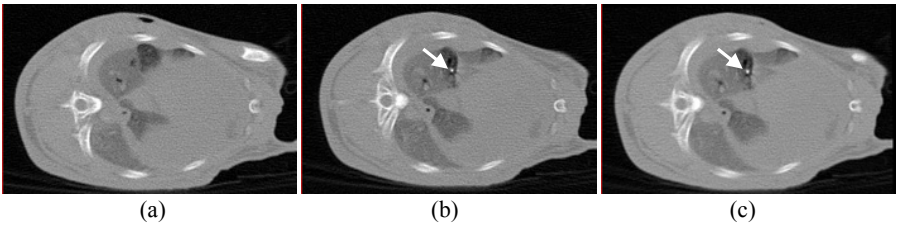

Fig. 5. An example of the intervention results. (a) The CT image with the tumor illustrated by the arrow before the puncture; (b) The confirmation CT after the puncture, and the arrow points indicates the needle tip; (c) The registered CT image of (b) to (a).

We did the experiments in eight rabbits, and they were numbered in the experiment time sequence. The first three experiments were performed without breath holding, while the later five were breath holding (by removing the ventilator) cases. We used distance between the target point in the pre-CT and the needle tip location in the confirmation CT (after global image registration using the FSL FLIRT program [17]) as the accuracy. Table 1 lists all the results. Overall the average distance without breath holding was 11*mm*, and the average error for the later five experiments with breath holding was 3.5*mm*, which means the lung movement caused by the breathing would impact the accuracy of intervention. After using the breath holding procedure, the accuracy of puncturing could be improved up to 70%.

Table 1. Accuracy of intervention experiments

Rabbit	Resolution (mm)	Accuracy (mm)
1	(0.27,0.27,1.20)	12.45
2	(0.26,0.26,1.20)	10.68
3	(0.29,0.29,1.20)	10.32
4	(0.28,0.28,1.20)	2.93
5	(0.23,0.23,1.20)	4.90
6	(0.28,0.28,1.20)	4.84
7	(0.28,0.28,1.20)	1.25
8	(0.25,0.25,1.20)	3.67

3.3 Quantitative Molecular Imaging Analysis

For validating the effectiveness of the microendoscopic procedure, we collected thirty microendoscopy video clips from the six rabbits' lung tumor to test the precision of our system. Fig. 6 shows the fluorescence microendoscopy images captured during our preliminary studies in the rabbit experiments. The motion of the image sequences

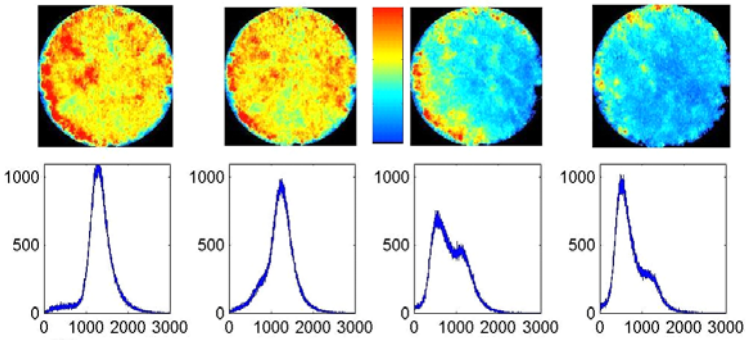

Fig. 6. Examples of the optical imaging of the rabbit experiments. Top: Four frames from the video. Bottom: histogram of images within a sliding time window (1 sec).

has been corrected, and the intensities are color-coded for better visualization. The histogram of the images within a one-second sliding window at each timepoint is shown in the second row. The first two frames show the molecular imaging results

within the tumor and the next two gives the picture at the boundary of the tumor. From the histograms we can see that the intensity distributions of the images within a temporal sliding window are different within and outside the tumor, and there is a significant different contrast or distribution difference between images with non-labeled tissue and $\alpha_v\beta_3$-labeled tissue, where the histograms' peak value of non-labeled tissue images is around 500, and that of $\alpha_v\beta_3$-labeled tissue images is around 1500. Hence these histograms could be classified into two different groups with threshold value 1000 in order to determine whether the molecular imaging generates a positive response. We plan to establish the diagnostic criteria and extensively validate them in the lung cancer patient experiments.

3.4 Discussion

The advantage of MIMIG is that it could provide a convenient, efficient and accurate interventional tool for possible on-the-spot diagnosis and treatment, and it will gain more diagnostic power if a contrast agent is approved by FDA for human use in the future. Currently, the fine needle aspiration biopsy guided by MIMIG can be used to diagnose cancer for human, where the radiofrequency ablation can also be applied for confirmed cancerous cases. We plan to validate the MIMIG system in biopsy and RFA of peripheral lung cancer patients and to evaluate the clinical outcomes by comparing the group using MIMIG and the traditional repetitive CT-guided procedures.

Respiratory motion is always important especially for lung applications. In this system we use breath holding strategy to minimize the motion or image changes during intervention. We are currently working on an improved deformable image registration tool that not only models the temporal respiratory motion but also estimate the image according to the movement of the fiducials and respiratory belt. This motion also affects the stability of the microendoscopy imaging. In addition to the motion correction functions reported in this paper, the future work also focuses on modeling the intensity variations in molecular imaging caused by such motion.

4 Conclusion

In this paper, a MIMIG intervention system is designed for lung tumor intervention and molecular imaging diagnosis. After successfully targeting the tumor, molecular imaging can be used for onsite diagnosis, which could be followed by radio-frequency ablation treatment. The benefit of a 3D image-guided platform system relies in the design and planning of the needle trajectory for puncture using an orthogonal viewer (simultaneous axial, sagittal, and coronal view), which provides a clear perspective about the depth and the direction of the needle for reaching the tumor. The pilot study on eight rabbits showed the feasibility of on-the-spot intervention and tumor diagnosis. In the future work, we will evaluate the MIMIG system using lung cancer patient intervention experiments.

References

1. McWilliams, A., MacAulay, C., Gazdar, A.F., Lam, S.: Innovative Molecular and Imaging Approaches for the Detection of Lung Cancer and Its Precursor Lesions. Oncogene. 21(45), 6949–6959 (2002)
2. Wardwell, N.R., Massion, P.P.: Novel Strategies for the Early Detection and Prevention of Lung Cancer. Seminars in oncology 32(3), 259–268 (2005)
3. Hicks, R.J., Lau, E., Alam, N.Z., Chen, R.Y.: Imaging in the Diagnosis and Treatment of Non-Small Cell Lung Cancer. Respirology (Carlton, Vic.) 12(2), 165–172 (2007)
4. Bach, P.B., Jett, J.R., Pastorino, U., Tockman, M.S., Swensen, S.J., Begg, C.B.: Computed Tomography Screening and Lung Cancer Outcomes. Jama 297(9), 953–961 (2007)
5. Wong, K., Liu, J., Tung, C.H., Wong, S.T.: In Vivo Molecular Microendoscopy in Human Lung Cancer Mouse Model. In: World Molecular Imaging Congress, Montreal, Canada (2009)
6. Krucker, J., Xu, S., Glossop, N., Viswanathan, A., Borgert, J., Schulz, H., Wood, B.J.: Electromagnetic Tracking for Thermal Ablation and Biopsy Guidance: Clinical Evaluation of Spatial Accuracy. J. Vasc. Interv. Radiol. 18(9), 1141–1150 (2007)
7. Frantz, D.D., Wiles, A.D., Leis, S.E., Kirsch, S.R.: Accuracy Assessment Protocols for Electromagnetic Tracking Systems. Physics in medicine and biology 48(14), 2241–2251 (2003)
8. Barratt, D.C., Davies, A.H., Hughes, A.D., Thom, S.A., Humphries, K.N.: Optimisation and Evaluation of an Electromagnetic Tracking Device for High-Accuracy Three-Dimensional Ultrasound Imaging of the Carotid Arteries. Ultrasound in medicine & biology 27(7), 957–968 (2001)
9. Milne, A.D., Chess, D.G., Johnson, J.A., King, G.J.: Accuracy of an Electromagnetic Tracking Device: A Study of the Optimal Range and Metal Interference. Journal of biomechanics 29(6), 791–793 (1996)
10. Banovac, F., Tang, J., Xu, S., Lindisch, D., Chung, H.Y., Levy, E.B., Chang, T., McCullough, M.F., Yaniv, Z., Wood, B.J., Cleary, K.: Precision Targeting of Liver Lesions Using a Novel Electromagnetic Navigation Device in Physiologic Phantom and Swine. Medical physics 32(8), 2698–2705 (2005)
11. Zhu, X., Xue, Z., Gao, X., Zhu, Y., Wong, S.T.C.: Voles: Vascularity-Oriented Level Set Algorithm for Pulmonary Vessel Segmentation in Image Guided Intervention Therapy. In: IEEE International Symposium on Biomedical Imaging: From Nano to Macro, ISBI 2009, Boston, pp. 1247–1250 (2009)
12. Xue, Z., Wong, K., Wong, S.T.: Joint Registration and Segmentation of Serial Lung Ct Images for Image-Guided Lung Cancer Diagnosis and Therapy. Comput. Med. Imaging Graph. 34(1), 55–60 (2010)
13. Ayvaci, A., Freedman, D.: Joint Segmentation-Registration of Organs Using Geometric Models. In: IEEE Eng. Med. Biol. Soc., pp. 5251–5254. IEEE Press, New York (2007)
14. Droske, M., Rumpf, M.: Multiscale Joint Segmentation and Registration of Image Morphology. IEEE transactions on pattern analysis and machine intelligence 29(12), 2181–2194 (2007)
15. Pohl, K.M., Fisher, J., Grimson, W.E., Kikinis, R., Wells, W.M.: A Bayesian Model for Joint Segmentation and Registration. NeuroImage 31(1), 228–239 (2006)
16. Rueckert, D., Sonoda, L.I., Hayes, C., Hill, D.L., Leach, M.O., Hawkes, D.J.: Nonrigid Registration Using Free-Form Deformations: Application to Breast Mr Images. IEEE transactions on medical imaging 18(8), 712–721 (1999)
17. Denton, E.R., Sonoda, L.I., Rueckert, D., Rankin, S.C., Hayes, C., Leach, M.O., Hill, D.L., Hawkes, D.J.: Comparison and Evaluation of Rigid, Affine, and Nonrigid Registration of Breast Mr Images. Journal of computer assisted tomography 23(5), 800–805 (1999)